Focal-plane wavefront sensors for direct exoplanet imaging: theory, simulations and on-sky demonstrations

Bos, S.P.

1 | Introduction

1.1 Detecting exoplanets

Major discoveries in astronomy have regularly led to paradigm shifts. Such a shift occurred when Galileo Galilei pointed his home-made telescope towards the skies and observed that Venus goes through a full set of phases that are similar to that of the Moon. This was evidence that Venus orbits the Sun, and therefore strengthened the case of the heliocentric model. When future astronomers discover life on an exoplanet, a planet orbiting another star, this will undoubtedly also change the view of humanity on its place in the universe. For centuries people have philosophized about the possibility of alien life on other worlds in the universe. This intriguing subject inspired people to actually prove the existence of these worlds. William Stephen Jacob, the director of Madras observatory, already claimed in 1855 to have discovered an exoplanet in orbit around the binary system 70 Ophiuchi (Jacob, 1855). This claim, and many others that followed throughout the 19th and 20th centuries, were subsequently refuted, usually because there was some systematic error that was not included in the initial analysis.

At the end of the 20th century, various technological developments enabled instruments to finally reach the required precision to actually detect an exoplanet. In 1992, two exoplanets were found to orbit the pulsar PSR B1257+12 (Wolszczan & Frail, 1992), a stellar remnant from a supernova. Three years later, in 1995, Michel Mayor and Didier Queloz announced the discovery of 51 Pegasi b, the first detected exoplanet orbiting a sun-like star (Mayor & Queloz, 1995). These discoveries were completely unexpected, as these two exoplanetary systems are so different than the solar system. Many astronomers did not expect to find exoplanets around pulsars, because they thought that exoplanets could not survive the supernova that precedes to the formation of the pulsar, and thus were surprised by the exoplanets orbiting PSR B1257+12. Astronomers also did not expect to find exoplanets close to their host stars, and yet 51 Pegasi b has an orbital period of just over four days, placing it closer to its host star than Mercury is to the Sun. Since then, over a quarter of a century later, exoplanet science has become a flourishing research field. At the time of writing this thesis, more than 4300 exoplanets have been discovered[1], and tens of thousands are waiting to be seen by the Gaia satellite (Lindegren et al., 2007; Perryman et al., 2014), and over a thousand by the Transiting Exoplanet Survey Satellite (TESS; Barclay et al. 2018; Ricker et al. 2014). The already accumulated wealth of information has taught us much about the exoplanet population. For example, we have inferred from extended surveys that ~22% of the sun-like stars harbors an Earth-like exoplanet in an orbit such that liquid water can exist on its surface (Petigura et al., 2013; Winn & Fabrycky, 2015). However, much remains to be discovered before we can confirm that these Earth-like exoplanets are actually habitable. We have to detect water, study the atmospheric pressure to determine if an ocean can be sustained, and measure the atmospheric composition to inform us about (bio)chemical processes occurring on the exoplanet. By studying the surface properties we will be able to distinguish between exoplanets domi-

[1] To be precise, at the moment of writing, January 26, 2021, there are 4331 confirmed exoplanet discoveries. Source: `https://exoplanets.nasa.gov`

nated by oceans or land mass.

The existence of most of the current, and the to be discovered exoplanets is inferred by indirect methods. That means that the exoplanet itself is not directly seen, but its effect on the host star. There are three main indirect methods of discovering exoplanets:

- **Radial velocity method**: Mayor and Queloz made their discovery with the ELODIE spectrograph (Baranne et al., 1996) by carefully measuring the radial velocity of 51 Pegasi over the course of hours, days and weeks. The radial velocity is found by measuring Doppler shifts in the star's spectrum. Any periodicity in the radial velocity indicates that there is an unknown body that pulls on the star while making its orbit (Struve, 1952). Analyzing the radial velocity as a function of time yields many of the exoplanet's orbital parameters. The amplitude of the signal gives a lower limit of the exoplanet's mass, and when the inclination of the orbit is known, its true mass can be calculated. The radial velocity method is responsible for exoplanet candidate detections around the closest neighbor of the Sun, Proxima Centauri (Anglada-Escudé et al., 2016; Damasso et al., 2020).
- **Transit photometry method**: A small fraction of exoplanets pass right in front of their star. This reduces the brightness of the star by a small fraction. If regular brightness dips are observed over long periods of time, then this is a strong indication of an exoplanet (Henry et al., 1999). The duration between dips and the shape of the brightness curve during transit contain information on the orbital parameters. Furthermore, the fraction of starlight that is blocked by the exoplanet is directly related to its radius. Using transit spectroscopy, the composition of the exoplanet's atmosphere can be measured. Transit photometry is responsible for the greatest number of exoplanet discoveries, the Kepler space-observatory alone has discovered over 3000 new exoplanets (Borucki et al., 2010).
- **Astrometry method**: When an exoplanet moves through its orbit, it causes a reflex motion of the star. The radial component of this motion is measured by the radial velocity method, and the lateral components are measured by the astrometry method. The astrometry method carefully measures the position of the star in the sky over a long period of time. A careful analysis of the time series of the star's position can, again, reveal orbital parameters of the exoplanet and its mass. The method's greatest achievement thus far is the measurement of the mass of Beta Pictoris b (Snellen & Brown, 2018), however, when the Gaia satellite's full dataset becomes available (Brown et al., 2018, 2016), over ten thousand exoplanet discoveries are expected.

When these methods are combined, they give a detailed view of the exoplanet's orbit, mass and radius. However, they are rather limited in characterizing the exoplanet's atmosphere and surface, of which the properties are far more interesting in the context of habitability and signs of life.

The direct imaging method is far more promising for exoplanet characterization as it aims to spatially separate the exoplanet's light from that of the star. This allows for a

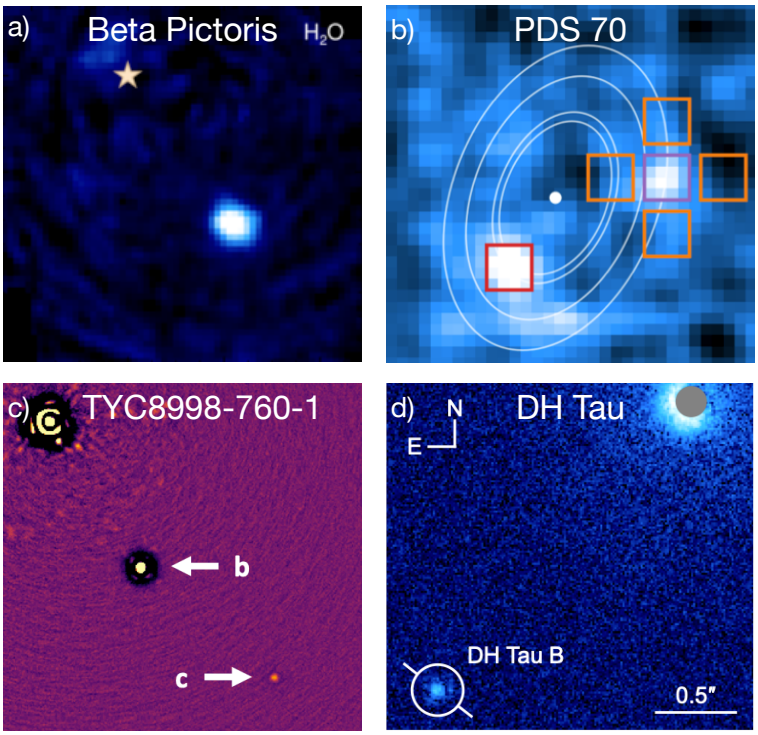

Figure 1.1: Images of exoplanets. a) Detection of H_2O in the atmosphere of Beta Pictoris b. Adopted from Hoeijmakers et al. (2018). b) Two accreting exoplanets in the disk around PDS 70. Adopted from Haffert et al. (2019). c) Two planets orbiting the solar-type star TYC8998-760-1. Adopted from Bohn et al. (2020). d) Polarized intensity image of the DH Tau system, revealing a disk around DH Tau b. Adopted from van Holstein et al. (2021).

far more detailed view of the exoplanet, because the temporal, spectral and polarization properties of the planet light itself can be analyzed. For example, the medium-resolution integral-field spectrograph SINFONI (Eisenhauer et al., 2003) yielded strong detections of CO and H_2O in the atmosphere of Beta Pictoris b (Hoeijmakers et al., 2018), and a survey with the polarimetric imaging mode of SPHERE/IRDIS (De Boer et al., 2020; Langlois et al., 2014) detected signs of disks around young exoplanets (van Holstein et al., 2021). Furthermore, as direct imaging observations explore the entire close-in circumstellar environment, they provide a unique opportunity to study the interaction between circumstellar disks and exoplanets during planet formation. The most famous example is PDS 70 (Haffert et al., 2019; Keppler et al., 2018; Wagner et al., 2018). Modern ground-based direct imaging instruments are capable of imaging young jovian planets on outer solar system-like scales around nearby stars (Bohn et al., 2020; Chauvin et al., 2017; Macintosh et al., 2015; Marois et al., 2008). However, the exoplanet yield from surveys with the current suite of instruments (VLT/SPHERE Beuzit et al. 2019; Subaru/SCExAO Jovanovic et al. 2015b; Gemini/GPI Macintosh et al. 2014) have been lower than predicted by models that extrapolated findings of indirect methods (Nielsen et al., 2019; Vigan et al., 2020). This led to motion multiple upgrade programs to improve the performance of these instruments, which will enable them to detect greater numbers of exoplanets (Boccaletti et al., 2020; Chilcote et al., 2018). Furthermore, new survey strategies have been developed that use input from the radial velocity and astrometry method to target stars that already show signs of the presence of a companion (Brandt et al., 2019; Currie et al., 2020a).

1.2 Direct imaging of exoplanets

The direct imaging technique is the most promising method to detect and characterize exoplanets and look for signs of life. Direct imaging has to overcome two fundamental challenges: **angular separation** and **contrast**. These challenges are the result of the wave-like nature of light. A star emits light as a spherical wave. When it arrives at Earth, it has effectively become a flat wavefront because of the large distances involved. When a space-based telescope captures the light, it cuts out part of the wavefront in the shape of its primary mirror. Due to diffraction and the finite extent and sharp edges of the telescope mirror, the image of the star is not infinitely sharp. The star looks like a central core of light surrounded by rings that become fainter with distance, but are still much brighter than exoplanets. This structure is referred to as the point spread function (PSF; Goodman 2005), and limits the angular resolution of the telescope ($\Delta\theta$) to:

$$\Delta\theta = 1.22\frac{\lambda}{D}, \tag{1.1}$$

with λ the wavelength and D the telescope diameter. An 8-meter class telescope operating at 1 μm has a resolution limit of ~0.03 arcsec. Suppose that we want to observe the Earth orbiting the Sun from a distance of 10 pc in the visible (~0.3-1 μm). At maximum separation, the angular separation between the two objects would be ~0.1 arcsec. The brightness ratio between the Earth and the Sun, referred to as contrast, is $\sim 10^{-10}$ (Traub & Oppenheimer, 2010). Due to this extreme contrast, direct imaging is regularly referred

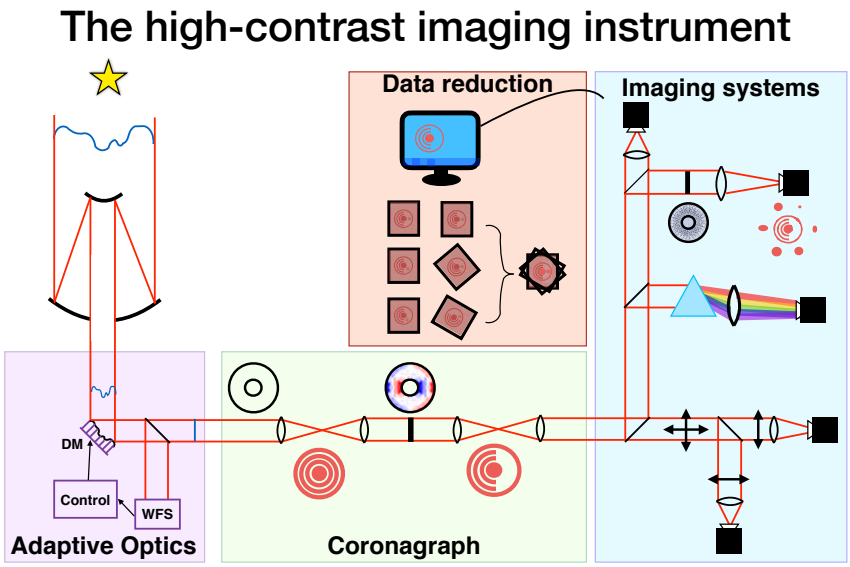

Figure 1.2: Schematic overview of a high-contrast imaging instrument. Acronyms in the figure are: DM = deformable mirror, WFS = wavefront sensor. Image courtesy of David Doelman.

to as **high-contrast imaging** (HCI).

Ground-based telescopes face an additional challenge posed by the Earth's atmosphere. Turbulence within the atmosphere causes wavefront aberrations in the light propagating through it, distorting the PSF and degrading the resolution achieved by the telescope significantly. To enable direct imaging of exoplanets with ground-based telescopes, these wavefront aberrations need to measured and corrected.

To overcome these challenges, HCI instruments are complex optical systems. They consist of multiple subsystems designed to correct wavefront aberrations, suppress starlight and analyze exoplanet light. Figure 8.2 shows a schematic of a ground-based HCI instrument. Light from the star is distorted by the Earth's, turbulent atmosphere before being captured by the telescope. The first subsystem is the adaptive optics (AO) system that measures and optically corrects wavefront aberrations. The coronagraph subsequently suppresses the starlight such that exoplanets can be observed and feeds the residual starlight and exoplanet light to various imaging systems. These imaging systems use various observing strategies to separate the residual starlight from the planet during data reduction. The exoplanet is then characterized by analyzing the spectrum and polarization state of light. The subsystems and other challenges in high-contrast imaging will be discussed in the following subsections.

1.2.1 Wavefront aberrations

HCI instruments are always limited by uncorrected wavefront aberrations. These wavefront aberrations create **speckles**, which are stellar PSF structures that closely mimic the exoplanet's signal. This noise source is referred to as **speckle noise** (Racine et al., 1999). Wavefront aberrations are deviations from the ideal wavefront that would otherwise generate a perfect PSF. Usually, wavefront aberrations are described in the pupil plane of the optical system and are divided into phase and amplitude aberrations. Phase aberrations result in a rugged wavefront, and when there are no phase aberrations, the wavefront is perfectly flat. Amplitude aberrations are intensity variations over the wavefront, and when not present, the wavefront has uniform intensity. Phase aberrations usually have a much stronger impact on the image than amplitude aberrations.

For ground-based observations, we can distinguish three important sources of wavefront aberrations.

Atmospheric turbulence
Before the light is captured by the telescope, it propagates through the Earth's atmosphere, which distorts the wavefront. When left uncorrected, starlight is spread over a larger area, degrading the resolution of the telescope to $\sim \lambda/r_0$, with r_0 the Fried parameter describing the spatial scale over which the root-mean-square wavefront error is less than 1 radian (Fried, 1966). For λ = 500 nm, r_0 is usually about 10 - 15 cm (Hardy, 1998) for a good site at night, and results in a deterioration of the angular resolution of an 8-meter class telescope by a factor $\sim 50 - 80$. The Fried parameter increases with wavelength, $r_0 \propto \lambda^{\frac{6}{5}}$ (Hardy, 1998), and therefore HCI observations in the visible light are more challenging than in the mid infrared. The atmosphere evolves over a timescale $\tau_0 \sim r_0/v$ (Greenwood, 1977), with v the wind speed. Therefore, speckles generated by atmospheric turbulence have a typical lifetime of milliseconds (Macintosh et al., 2005). Atmospheric phase aberrations are dominant over atmospheric amplitude aberrations (also referred to as scintillation) for large telescopes (Guyon et al., 2018). However, amplitude aberrations can become relevant during HCI observations when they correlate with phase aberrations, leading to the asymmetric wind-driven halo (Cantalloube et al., 2018, 2020).

Telescope effects
The telescope is also a cause of wavefront aberrations. It is mainly related to temperature differences between the telescope and the surrounding air. Mirror seeing occurs when the temperature of the telescope's primary mirror is different to that of the surrounding air (Tallis et al., 2020). The warm mirror leads to natural convection, which is turbulent, directly in the path of the incoming light and thus degrading the wavefront. Another effect is the low-wind effect (LWE; Sauvage et al. 2015; Sauvage et al. 2016; Milli et al. 2018). The LWE occurs when the ground wind speed is very low (under a few m/s), which otherwise would be considered to be amongst the best observing conditions. It has now been well understood to be caused by radiative heat exchange between the telescope structure and night sky (Holzlöhner et al., 2020). When the dome opens for observations, it exposes the telescope structure to the night sky, resulting in rapid radiative cooling of the structure

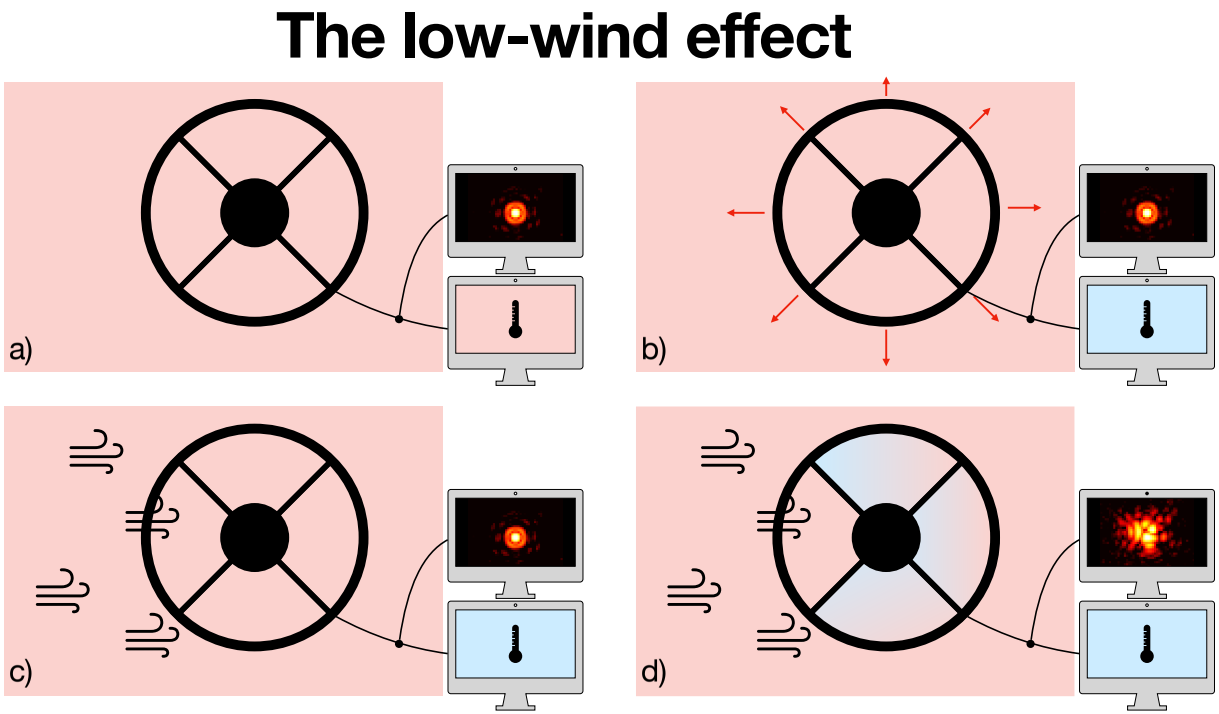

Figure 1.3: Explanation of the low-wind effect (LWE). a) Before observations, the telescope and surrounding air have the same temperature. b) When the dome opens, the telescope is exposed to the night sky. Depending on the mass, the heat capacity and the emissivity of the particular part of the telescope, it can rapidly cool down by radiative transfer. c) Air is flowing over the structure with a low wind speed. d) The air in contact with the spider rapidly cools down and changes its refractive index. Resulting in a sharp OPD step over the spider that is not easily seen by the wavefront sensor, but strongly distorts the PSF.

to a temperature below that of the ambient air. An example of this happening with the secondary mirror support structure (or spiders) is illustrated in Figure 1.3. Air flows over the cold spiders with a low wind speed. The air in contact with the spider rapidly cools down and changes its refractive index. This introduces a sharp optical path length difference (OPD) between light passing on opposite sides of a spider, which strongly distorts the PSF. The aberrations generated by the LWE were measured to have a peak-to-valley wavefront error of up to hundreds of nanometers (Sauvage et al., 2015) and evolve on timescales of seconds (Milli et al., 2018). Typical AO systems have difficulties measuring and correcting the LWE, and therefore the LWE is one of the limitations to the direct imaging of exoplanets at small angular separations.

Instrumental aberrations
Usually, the first sub-system within the HCI instrument is the AO system (Figure 8.2), which measures and corrects upstream wavefront aberrations. However, optics downstream of the wavefront sensor also introduce wavefront aberrations due to optical misalignments, manufacturing errors and internal seeing. These aberrations are not sensed by the main wavefront sensor, but do affect the optical quality of the imaging system, and are referred to as **non-common path aberrations** (NCPA). Due to temperature, humidity and gravitational vector changes, NCPA slowly evolve over timescales of minutes and hours (Goebel et al., 2018; Martinez et al., 2013, 2012; Milli et al., 2016). NCPA generate quasi-static speckles that are especially challenging to remove in post-processing and are one of the current limitations in HCI (Hinkley et al., 2007).

1.2.2 Adaptive optics

The subsystem that deals with wavefront aberrations is the AO system. It consists of a wavefront sensor (WFS) positioned behind a deformable mirror (DM) as shown in Figure 8.2. A real-time control system converts WFS measurements into DM actuator displacements in a closed-loop configuration. For the purpose of detecting exoplanets, the AO system needs to deliver extremely high wavefront quality, and is therefore regularly referred to as extreme AO (XAO; Guyon 2018). The XAO system needs to operate fast enough to keep up with the atmosphere and runs typically at kHz (Greenwood, 1977).

The DM is a reflective optic that can change its shape very precisely at a high frequency (Madec, 2012). The WFS estimates the wavefront from intensity measurements by means of optical manipulations. Currently, the most common WFSs are the Shack-Hartmann WFS (SH-WFS; Hartmann 1900; Shack 1971) and the Pyramid WFS (PyWFS; Ragazzoni 1996). The latter being more sensitive, but requires that the magnitude of the wavefront aberrations is smaller. The sensitivity of the WFS plays an important role in the on-sky contrast (Guyon, 2005), and therefore the current generation of HCI instruments is transitioning towards the PyWFS.

A limitation of these WFSs is the island effect (IE; Le Louarn et al. 2013). The IE occurs when the telescope pupil is strongly fragmented by the spiders supporting the secondary mirror, as shown in Figure 1.4. When the spiders become too wide, the SH-WFS and

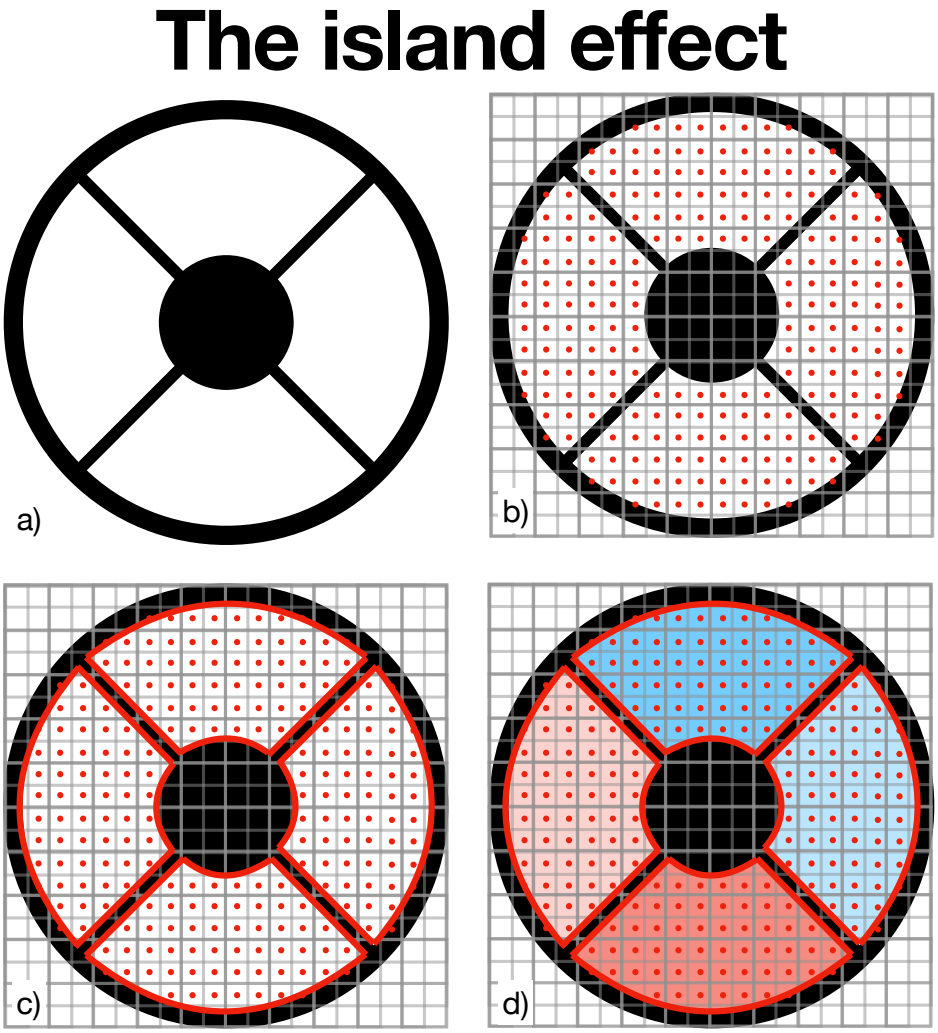

Figure 1.4: Explanation of the island effect using a SH-WFS. a) The telescope pupil with shadows of the secondary mirror and its support structure. The beams of the support structure are referred to as the spiders. b) An array of microlenses is placed over the pupil and generates spots on the detector used for wavefront sensing (the red dots). The position of the spots indicates the local gradient of the wavefront. c) The wavefront is reconstructed by integrating over the wavefront gradient measurements of adjacent spots. However, because the spiders cover some microlenses, the wavefront can only be reconstructed within four “islands”. d) When an aberration with sharp phase discontinuities over the spiders occurs, for example the LWE (Figure 1.3), the WFS can not accurately measure the discontinuity. This leads to unmeasured and thus uncorrected wavefront errors.

PyWFS poorly sense sharp discontinuities in the wavefront across these gaps. This is because these WFSs measure the gradient of the wavefront in two orthogonal directions. The wavefront is reconstructed by stitching together these gradient measurements. When there is a discontinuity in the gradient measurements due to a spider, it can be difficult to accurately reconstruct the wavefront. The IE is the reason that the WFSs such as the SH-WFS and PyWFS have difficulties with measuring the LWE. Another limitation is that the WFS only measures aberrations upstream of its position in the optical train, and (significant) NCPA are left unmeasured and uncorrected. To this end, additional WFSs downstream of the AO system have been developed. These WFSs use either the starlight rejected light by the coronagraph (Singh et al., 2017, 2014, 2015), very sensitive WFS designs complementary to the SH- and PYWFS (Doelman et al., 2019; N'Diaye et al., 2013, 2016; Vigan et al., 2019), or the science focal plane (Jovanovic et al., 2018). Focal-plane wavefront sensing is the most promising solution as it completely eliminates NCPA, and is amongst the most sensitive wavefront sensing solutions (Guyon, 2005). It is also the main subject of this thesis, and a more extensive introduction on focal-plane wavefront sensing is presented in section 1.3.

1.2.3 Coronagraphy

The AO system feeds the light to the coronagraph. The goal of the coronagraph is to suppress the starlight while transmitting the exoplanet light. Furthermore, it also reduces speckle noise, because bright diffraction structures, to which some speckles are otherwise 'pinned', are removed (Bloemhof et al., 2001; Soummer et al., 2007).

Over the years many different coronagraph concepts have been proposed (Mawet et al., 2012; Ruane et al., 2018). These concepts can be roughly divided into two categories:

- **Focal-plane coronagraphs**: A focal-plane optic is placed on the on-axis star and either absorbs the starlight or diffracts it outside of the downstream pupil by either amplitude (Lyot, 1939) or phase manipulation (Roddier & Roddier, 1997). An additional optic in the downstream pupil-plane, referred to as the Lyot stop, blocks the starlight. Because the exoplanet is spatially separated from the star, its light is only slightly attenuated and not diffracted outside the pupil and therefore is transmitted towards the detector. Additional pre-apodizers in de pupil-plane upstream of the focal-plane improve the rejection of the star (Aime et al., 2002; Por, 2020; Soummer et al., 2003). These coronagraphs offer very high contrasts with good exoplanet throughput, but are sensitive to vibrations and the finite diameter of the star.

- **Pupil-plane coronagraphs**: A pupil-plane optic shapes the PSF such that starlight is cancelled on one or two sides of the PSF by either amplitude (Kasdin et al., 2003) or phase manipulation (Codona & Angel, 2004). The region where the starlight is cancelled is referred to as the dark hole. As both the star and planet propagate through the coronagraph, the exoplanet will also acquire the coronagraphic PSF, spreading the exoplanet light over a larger area on the detector. However, these

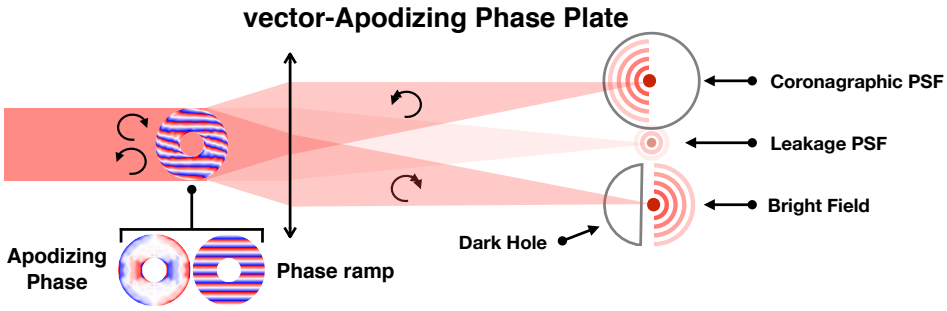

Figure 1.5: Schematic of the vAPP coronagraph. The coronagraphic PSFs are separated by a phase ramp that is includes into the phase design.

coronagraphs are completely insensitive to the finite diameter of the star, and are easily implemented into instruments.

Particularly relevant to this thesis is the vector-Apodizing Phase Plate (vAPP; Snik et al. 2012). The vAPP induces the required pupil-plane phase by means of the geometric phase (Berry, 1987; Pancharatnam, 1956) on opposite circular polarization states. The vAPPs geometric phase is introduced when the fast-axis angle of a half-wave retarder is spatially varying. The phase that is induced is twice the fast-axis angle, and is opposite for the opposite circular polarization states, which results in two coronagraphic PSFs with opposite dark holes. This is shown in Figure 1.5. Due to its geometric origin, the induced geometric phase is completely independent of wavelength, but the efficiency with which the phase is transferred to the light depends on the retardance offset from half wave. Light that does not acquire the desired phase is generally referred to as leakage, and in the case of the vAPP will form a non-coronagraphic PSF. High leakage will affect coronagraphic performance as light from the leaked PSF can contaminate the dark hole. Half-wave retarders with spatially varying fast-axis angle can be implemented with liquid-crystal technology (Escuti et al., 2016). Using a direct-write system, the desired fast-axis angle can be printed into a liquid-crystal photo-alignment layer that that has been deposited on a substrate (Miskiewicz & Escuti, 2014). To achromatise the half-wave retarder, several layers of carefully designed, self-aligning birefringent liquid crystals can be deposited on top of the initial layer (Komanduri et al., 2013). This technology has shown to achieve minimal leakage over a broad wavelength range (Doelman et al., 2020, 2017). In the simplest and most common implementation the two coronagraphic PSFs are spatially separated with a polarization-sensitive grating (Oh & Escuti, 2008) that is integrated into the phase design (Otten et al., 2014). These coronagraphs are mainly used for operation with narrowband filters or integral-field spectrographs. This is because diffraction effects scale with wavelength, and therefore, when observing in a broadband filter with a vAPP, the grating will smear the coronagraphic PSFs.

1.2.4 Observing strategies and post processing

Due to uncorrected atmospheric wavefront errors, ground-based HCI observations are limited to raw contrasts of $\sim 10^{-5}$ at a few λ/D (Guyon et al., 2012). Within the control radius the dominant noise sources are the finite time delay between measuring and correcting the wavefront, and photon noise in the wavefront sensor measurements. It is possible to detect and characterize exoplanets below this contrast level by separating the star and planet light with advanced post-processing methods. These methods use a known diversity in the dataset to either build up an estimate of the stellar PSF, which can then be subtracted from the individual images to reveal the exoplanet (Cantalloube et al., 2021), or use fundamental differences between the properties of star and planet light (e.g. spectrum, polarization or coherence). The observing strategy is designed to provide this diversity, and the following methods are either in use or being developed (presented in alphabetic order):

- **Angular differential imaging** (ADI; Marois et al. 2006a): During an observation, the sky, and therefore the exoplanet, is allowed to rotate over the detector while taking images. The orientation of the stellar PSF remains fixed over time. The PSF of the target star is then estimated from this time series.
- **Coherence differential imaging** (CDI; Guyon 2004): Stellar speckles are coherent with starlight, while the exoplanet light is incoherent. This is because exoplanet light originates from a spatially separated source. By measuring the coherence of the light on the detector, the light from the star and exoplanet are separated.
- **Orbit differential imaging** (ODI; Males et al. 2015): The target is observed multiple times with long periods of time in between them. The diversity is then provided by the movement of the exoplanet in its orbit.
- **Polarization differential imaging** (PDI; Kuhn et al. 2001): Starlight is unpolarized to a very high degree, while light reflected from the surface of the exoplanet is polarized. By adding a polarizing beam splitter to the HCI instrument, the polarization state of the incident light can be measured and the star and planet light separated.
- **Reference star differential imaging** (RDI; Smith & Terrile 1984): Another star, with the same spectral properties as the target star and without companions, is observed with the same instrument and telescope settings. The PSF of the target star is estimated with these images.
- **Spectral differential imaging** (SDI; Sparks & Ford 2002): Due to temperature and atmospheric composition differences, the spectrum of the star and and exoplanet light are different. By measuring the spectrum of the light, the star and exoplanet are separated.

It is also possible and advantageous to combine several of these observation strategies (Christiaens et al., 2019; van Holstein et al., 2017).

PDI and SDI have the additional advantage that they simultaneously act as characterization diagnostic. Observations by medium- and high-resolution integral-field spectrographs can be used to detect atomic and molecular lines from an exoplanet's atmosphere (Bowler et al., 2019; Snellen et al., 2015). Using polarimetry, it is possible to study cloud structures in the exoplanet's atmosphere (De Kok et al., 2011; Stam et al., 2004), and circumplanetary disks (Stolker et al., 2017). Combining both techniques in spectropolarimetric observations enables constraints on water clouds and oceans (Karalidi et al., 2012), and even (maybe) measure biological activity (Patty et al., 2019).

1.2.5 Detecting exoplanet variability

Like the majority of the planets in the solar system, exoplanets are expected to have clouds in their atmospheres (Helling, 2019). Detecting and studying clouds on exoplanets will improve our understanding of the atmospheric composition and weather systems on these other worlds. Brown dwarfs have cloud structures (Cooper et al., 2003), that express themselves in brightness variations while the object rotates (Apai et al., 2013; Eriksson et al., 2019; Metchev et al., 2015). Exoplanets are expected to exhibit similar variability (Apai et al., 2019; Biller, 2017; Kostov & Apai, 2012). Thus far, variability has only been observed with the extremely stable Hubble Space Telescope (HST) for the exoplanet 2M1207b, which has photometric variations at the 0.78-1.36% level (Zhou et al., 2016). Ground-based observations of HR 8799 with VLT/SPHERE have not yet led to conclusive detections of variability (Apai et al., 2016; Biller et al., 2021).

Observing exoplanet variability is not trivial because most coronagraphs occult the host star, which is usually the direct photometric reference. This makes it challenging to disentangle exoplanet variability from seeing and transmission changes in the Earth's atmosphere. To overcome this problem, Marois et al. (2006b) and Sivaramakrishnan & Oppenheimer (2006) introduced diffractive methods to generate artificial speckles that serve as photometric references. These methods apply static phase or amplitude modulations in the pupil plane before the coronagraph's focal-plane optic. The artificial speckles are designed to not be occulted by the coronagraph. An additional advantage is that the reference speckles can be closer to the exoplanet in intensity, which prevents possible issues with saturation and detector non-linearities. Current HCI instruments implement these artificial speckles either with a square grid that acts as an amplitude grating (Gemini/GPI; Wang et al. 2014), or with a static DM modulation (VLT/SPHERE; Langlois et al. 2013). However, the limiting factor of these solutions is their coherency with the time-varying speckle background, which results in interference that dynamically distorts the shape and brightness of the artificial speckles. This in turn ultimately limits their photometric precision (Jovanovic et al., 2015a). The origin of these background speckles has been extensively discussed in subsection 1.2.1. Subaru/SCExAO circumvents this problem by high-speed, temporal DM modulation that switches ($<$ 1 ms) the phase of the artificial speckles between 0 and π (Jovanovic et al., 2015a). Due to the modulation, the interference averages out, and the artificial speckles effectively become incoherent, increasing their precision by a factor of between two and three. Recently, a more advanced method was presented that also alternates the position of the speckles, allowing for accu-

rate background estimation, improving the photometric precision to < 1% for 80 second exposures (Sahoo et al., 2020).

1

1.3 Focal-plane wavefront sensing

As discussed in the above sections, one of the current limitations in high-contrast imaging are non-common path aberrations (NCPA). NCPA originate from misalignments, fabrication errors, and temperature changes in the optics and internal turbulence downstream of the system's main WFS. In subsection 1.2.1 we have seen that they slowly evolve with time, which makes their removal in post-processing very challenging. The best solution is to measure NCPA using the science detector located in the focal plane, and optically correct them with a DM. We define focal-plane wavefront sensing (FPWFS) as follows.

Focal-plane wavefront sensing

is estimating the pupil-plane or focal-plane electric field by means of measurements with the science camera (or equivalent) placed in the focal plane.

In this section we introduce the theory behind focal-plane wavefront sensing, discuss the challenges and cluster the different focal-plane wavefront sensors into different families.

1.3.1 Theory

The fundamental problem in FPWFS is, with the current detector technology, that we do not have direct access to the focal-plane electric field, but instead measure the focal-plane intensity. The result is that only the focal-plane amplitude can be recovered and not the focal-plane phase. This is shown by the following equations:

$$E_{\text{foc}} = A_{\text{foc}} e^{i\theta_{\text{foc}}}, \tag{1.2}$$

$$I_{\text{foc}} = |E_{\text{foc}}|^2 \tag{1.3}$$

$$= A_{\text{foc}}^2, \tag{1.4}$$

with A_{foc} the amplitude and θ_{foc} the phase of the focal-plane electric field (E_{foc}), and I_{foc} the focal-plane intensity. To retrieve the amplitude **and** the phase, we have to manipulate E_{foc} such that these parameters are encoded in the intensity signal. In this subsection we will identify the requirements on pupil-plane manipulations that enable measuring pupil-plane phase with focal-plane images.

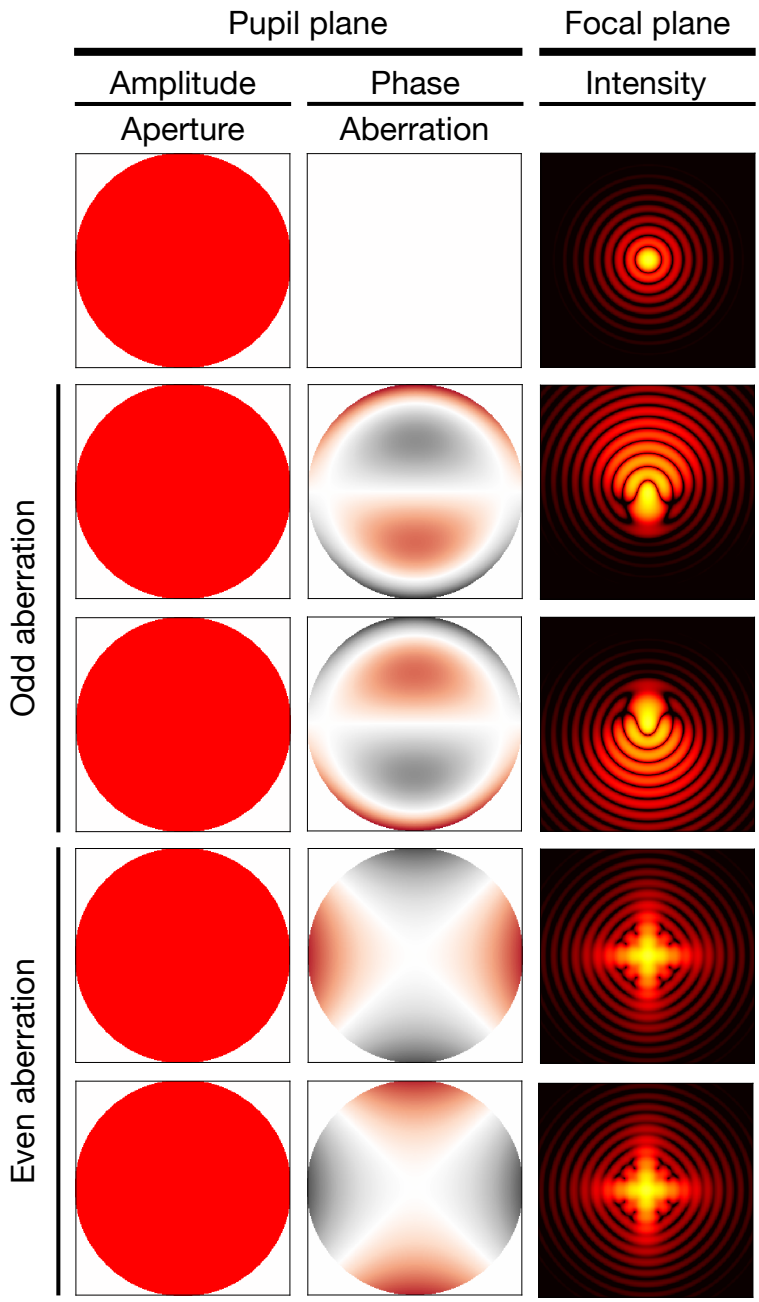

Figure 1.6: Effect of sign changes of even and odd pupil-plane phase aberrations on the PSF. The PSF is formed by an even aperture, and the phase aberrations have a 1 radian root-mean-square wavefront error. The scales of the colormaps are the same for every column of images. The focal-plane intensity is shown in log scale.

To understand the challenge of estimating pupil-plane phase with focal-plane images, we simulate PSFs for a circular aperture with various wavefront aberrations (even and odd, and changing aberration sign). The results are presented in Figure 1.6. It shows that the sign of odd pupil-plane phase aberrations can be distinguished by observing the shape of the PSF. However, for even pupil-plane phase aberrations it is not possible to determine the sign, because the PSFs look identical for opposite signs. The only information that can be retrieved is the magnitude of the even phase aberration.

To understand the origin of this sign ambiguity, we start by writing the the pupil-plane electric field (E_{pup}) as follows:

$$E_{\text{pup}} = A_{\text{pup}} e^{i\theta_{\text{pup}}} \tag{1.5}$$
$$= A_{\text{pup}} \cos(\theta_{\text{pup}}) + iA_{\text{pup}} \sin(\theta_{\text{pup}}), \tag{1.6}$$

with A_{pup} the pupil-plane amplitude and θ_{pup} the pupil-plane phase. The focal-plane electric field (E_{foc}) is formed by propagating E_{pup} using the Fraunhofer propagation operator $\mathcal{P}\{\cdot\} \propto \frac{1}{i}\mathcal{F}\{\cdot\}$ (Goodman, 2005), with $\mathcal{F}\{\cdot\}$ the Fourier transform.

$$E_{\text{foc}} = \mathcal{P}\{E_{\text{pup}}\} \tag{1.7}$$
$$= \mathcal{P}\{A_{\text{pup}} \cos(\theta_{\text{pup}})\} + \mathcal{P}\{iA_{\text{pup}} \sin(\theta_{\text{pup}})\} \tag{1.8}$$
$$= a + ib, \tag{1.9}$$

with a and b the real and imaginary parts of E_{foc}, respectively. The terms a and b generally consists of a mixture of $\mathcal{P}\{A_{\text{pup}} \cos(\theta_{\text{pup}})\}$ and $\mathcal{P}\{A_{\text{pup}} \sin(\theta_{\text{pup}})\}$, and as we will see, this depends on the symmetries of A_{pup} and θ_{pup}. The focal-plane intensity, or PSF, is given by:

$$I_{\text{foc}} = |E_{\text{foc}}|^2 \tag{1.10}$$
$$= a^2 + b^2. \tag{1.11}$$

Before we continue, we recall the following mathematical properties:

1. A function $f(r)$ can be decomposed into even (f_{even}) and odd (f_{odd}) functions:

$$f(r) = f_{\text{even}}(r) + f_{\text{odd}}(r), \tag{1.12}$$
$$f_{\text{even}}(r) = \frac{f(r) + f(-r)}{2}, \tag{1.13}$$
$$f_{\text{odd}}(r) = \frac{f(r) - f(-r)}{2}. \tag{1.14}$$

   This is useful, because even and odd function behave differently under the Fraunhofer propagation operator, which is shown in Table 2.1.

2. The composition and multiplication properties of even and odd functions:

$$f_{\text{even}}(r) \cdot g_{\text{odd}}(r) = h_{\text{odd}}, \tag{1.15}$$
$$f_{\text{odd}}(r) \cdot g_{\text{odd}}(r) = h_{\text{even}}, \tag{1.16}$$
$$f_{\text{even}}(r) \cdot g_{\text{even}}(r) = h_{\text{even}}, \tag{1.17}$$
$$f_{\text{even}}[g_{\text{odd}}(r)] = h_{\text{even}}, \tag{1.18}$$
$$f_{\text{odd}}[g_{\text{odd}}(r)] = h_{\text{odd}}, \tag{1.19}$$
$$f_{\text{odd}}[g_{\text{even}}(r)] = h_{\text{even}}, \tag{1.20}$$
$$f_{\text{even}}[g_{\text{even}}(r)] = h_{\text{even}}. \tag{1.21}$$

   These determine the symmetries of the real and imaginary terms of E_{pup} (Equation 7.1).

3. The symmetry properties of the Fraunhofer propagation are shown in Table 2.1. These determine how pupil-plane aberrations map to the real and/or imaginary terms of the focal-plane electric field.

4. Finally, the hermitian property of the Fraunhofer propagation. This states that a conjugated pupil-plane electric field $E'_{\text{pup}} = E^*_{\text{pup}}$ (i.e. a phase sign flip; * denotes the conjugation) results in a flipped and conjugated focal-plane electric field $E'_{\text{foc}} = \mathcal{P}\{E'_{\text{pup}}\}$:

$$E'_{\text{foc}} = -E_{\text{foc}}(-r)^*. \tag{1.22}$$

The reason that the symmetry decomposition, combined with the decomposition of E_{pup} into its real and imaginary components (Equation 7.1), is important is that the Fraunhofer propagation operator maps combinations of these decompositions into either real or imaginary components of E_{foc}, as shown in Table 2.1. Combined with the symmetries of the aperture, it determines whether a sign ambiguity will be present or not.

Now, suppose that the aperture is even ($A_{\text{pup}} = A_e$), which is true for most telescope apertures, and that we have an even phase aberration ($\theta_{\text{pup}} = \theta_e$). We then find the following pupil-plane electric field:

$$E_{\text{pup}} = A_e e^{i\theta_e} \tag{1.23}$$
$$= \underbrace{A_e \cos(\theta_e)}_{\text{even}} + i \underbrace{A_e \sin(\theta_e)}_{\text{even}}. \tag{1.24}$$

We note that only the imaginary term contains information on the sign of θ_e. Propagating E_{pup} to the focal plane yields (Table 2.1):

$$E_{\text{foc}} = \underbrace{a}_{\mathcal{P}\{iA_e \sin(\theta_e)\}} + \underbrace{ib}_{\mathcal{P}\{A_e \cos(\theta_e)\}} \tag{1.25}$$
$$I_{\text{foc}} = \underbrace{a^2}_{\text{even}} + \underbrace{b^2}_{\text{even}} \tag{1.26}$$

Table 1.1: Fraunhofer propagation symmetry properties (Goodman, 2005), these are the Fourier properties multiplied with a factor $-i$ ($E_{\text{foc}} = \mathcal{P}\{E_{\text{pup}}\} \propto \frac{1}{i}\mathcal{F}\{E_{\text{pup}}\}$).

Pupil-plane electric field $E_{\text{pup}} = A\cos(\theta) + iA\sin(\theta)$			Focal-plane electric field $E_{\text{foc}} = a + ib$	
Term	Term symmetry	A, θ symmetry	Term	Term symmetry
$A\cos(\theta)$	Even	$(A_{\text{even}}, \theta_{\text{even}})$, $(A_{\text{even}}, \theta_{\text{odd}})$	ib	Even
$A\cos(\theta)$	Odd	$(A_{\text{odd}}, \theta_{\text{even}})$, $(A_{\text{odd}}, \theta_{\text{odd}})$	a	Odd
$iA\sin(\theta)$	Even	$(A_{\text{even}}, \theta_{\text{even}})$, $(A_{\text{odd}}, \theta_{\text{odd}})$	a	Even
$iA\sin(\theta)$	Odd	$(A_{\text{even}}, \theta_{\text{odd}})$, $(A_{\text{odd}}, \theta_{\text{even}})$	ib	Odd

When the sign of the even aberration changes ($\theta_e \rightarrow -\theta_e$), we will not observe a change in I_{foc}. This is because a, which contains the sign information, is an even function, and therefore does not show a response under sign change.

We can do a similar calculation for an odd phase aberration ($\theta_{\text{pup}} = \theta_o$). Here we also assume that the aperture is even ($A_{\text{pup}} = A_e$). The pupil-plane electric field is then:

$$E_{\text{pup}} = \underbrace{A_e \cos(\theta_o)}_{\text{even}} + i \underbrace{A_e \sin(\theta_o)}_{\text{odd}} . \tag{1.27}$$

Again, the sign information carrying term is the imaginary part of the electric field. Calculating the focal-plane electric field and intensity we find:

$$E_{\text{foc}} = \underbrace{ib}_{\mathcal{P}\{A_e \cos(\theta_o) + iA_e \sin(\theta_o)\}} , \tag{1.28}$$

$$I_{\text{foc}} = b^2 \tag{1.29}$$

$$= \underbrace{\mathcal{P}\{A_e \cos(\theta_o)\}^2}_{\text{even}} + \underbrace{\mathcal{P}\{A_e \sin(\theta_o)\}^2}_{\text{even}} + \underbrace{2\mathcal{P}\{A_e \cos(\theta_o)\}\mathcal{P}\{A_e \sin(\theta_o)\}}_{\text{odd}} . \tag{1.30}$$

This calculation shows that in the case of odd phase aberrations, the real and imaginary parts of the pupil-plane electric field both map to the imaginary part of the focal-plane electric field. The result is that in the focal-plane intensity there is an interference term with odd symmetry that changes its shape under sign change. This interference term enables that sign changes of odd pupil-plane phase aberrations are observable in the PSF.

The previous calculations show that whether or not a sign ambiguity exists is determined by the presence of additional term that interferes with the sign carrying term. In Equation 1.25 we found that the sign information of even pupil-plane phase aberrations is located in the real part of the focal-plane electric field. Inspecting Table 2.1 shows that additional terms in the real part of the focal-plane electric field can be created by applying either a known odd pupil-plane amplitude, a known even pupil-plane phase, or a combination of both. These solutions correspond with well-known focal-plane wavefront sensing techniques. Phase diversity techniques apply even pupil-plane phase modes (Gonsalves, 1982; Paxman et al., 1992), and techniques such as the Asymmetric Pupil Fourier Wave-Front Sensor (APFWFS; Martinache 2013) and the differential Optical Transfer Functions wavefront sensor (dOTF; Codona 2013) use odd pupil-plane amplitude.

1.3.2 Family of focal-plane wavefront sensors

Many different FPWFSs have been developed over the years, each with their own unique implementation. A review is presented in Jovanovic et al. (2018). Here we aim to extend this review and categorize the different FPWFSs according to their method of breaking the sign degeneracy.

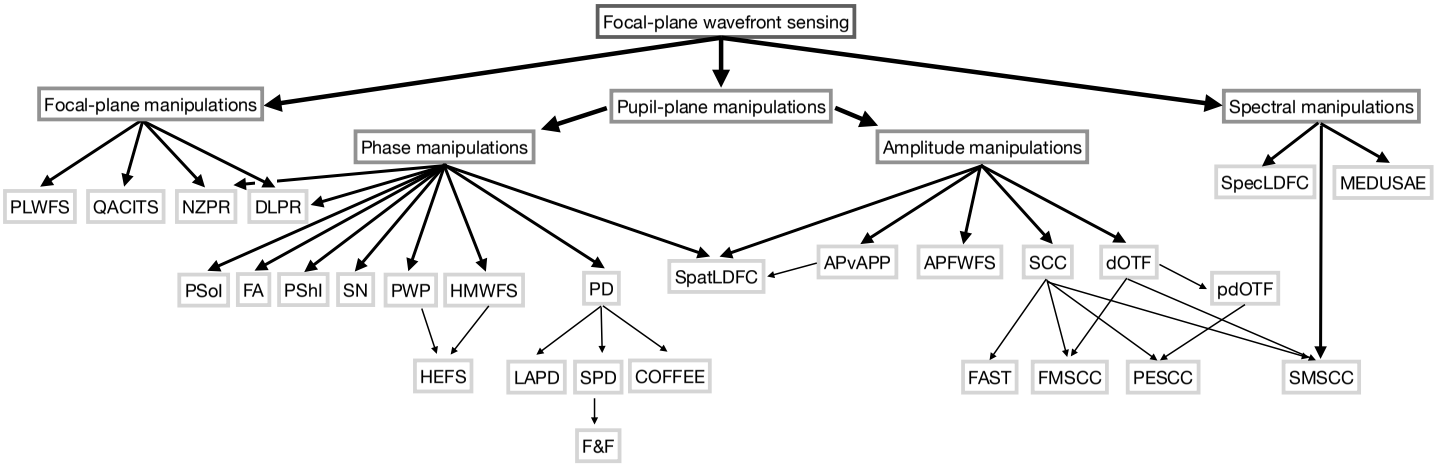

Figure 1.7: Acronyms in the figure are: **Focal-plane manipulations:** NZPR = Nijboer-Zernike Phase Retrieval, QACITS = Quadrant Analysis of Coronagraphic Images for Tip-tilt Sensing, PLWFS = Photonic Lantern WaveFront Sensor, DLPR = Deep Learning Phase Retrieval, **Pupil-plane phase manipulations:** PD = Phase Diversity, COFFEE = COronagraphic Focal-plane waveFront Estimation for Exoplanet detection, SPD = Sequential-phase diversity, F&F = Fast and Furious, LAPD = Linearized Analytical Phase Diversity, FA = Frazin Algorithm, PSoI = Phase Sorting Interferometry, PShI = Phase Shifting Interferometry, PWP = Pair-Wise Probing, SN = Speckle Nulling, HMWFS = Holographic Modal WaveFront Sensor, HEFS = Holographic Electric Field Sensor, **Pupil-plane amplitude manipulations:** spatLDFC = Spatial Linear Dark Field Control, APFWFS = Asymmetric Pupil Fourier WaveFront Sensor, APvAPP = Asymmetric Pupil vector-Apodizing Phase Plate, SCC = Self-Coherent Camera, FAST = Fast Atmospheric SCC Technique, FMSCC = Fast-Modulated Self-Coherent Camera, PESCC = Polarization-Encoded Self-Coherent Camera, SMSCC = Spectral-Modulated Self-Coherent Camera, dOTF = differential Optical Transfer Function, pdOTF = polarization differential Optical Transfer Function **Spectral manipulations:** SpecLDFC = Spectral Linear Dark Field Control, MEDUSAE = Multispectral Exoplanet Detection Using Simultaneous Aberration Estimation,

Figure 1.7 shows the family tree with, to our best knowledge, the FPWFSs currently used or being developed in HCI. Three distinct branches can be distinguished that each use a different kind of manipulation to break the sign ambiguity:

- **Focal-plane manipulation:** A device located in a focal-plane (e.g. a focal-plane coronagraph or photonic lantern) breaks the sign ambiguity by means of optical manipulations.
- **Pupil-plane manipulation:** The pupil-plane amplitude and/or phase are manipulated such that the sign ambiguity is broken for focal-plane intensity measurements.
- **Spectral manipulation:** The chromatic nature of aberrations is used to measure the wavefront.

We more extensively discuss the members of the families below.

Focal-plane manipulation
As mentioned above, the focal-plane manipulation branch uses optical devices in the focal plane to lift the phase ambiguity. The Quadrant Analysis of Coronagraphic Images for Tip-tilt Sensing (QACITS; Huby et al. 2015) is based on the analysis of the Vector Vortex Coronagraph (VVC; Mawet et al. 2005) images to infer the direction and magnitude of pointing errors. QACITS is regularly used for HCI observations with the Keck/NIRC2 (Huby et al., 2017). The VVC is a focal-plane coronagraph that induces an opposite vortex phase to opposite circular polarization states. The vortex phase is what breaks the sign ambiguity for even pupil-plane phase aberrations. Other techniques also use the diversity provided by the VVC, but are aimed to provide higher-order wavefront measurements. The Nijboer-Zernike Phase Retrieval method (NZPR; Riaud et al. 2012a) splits the opposite circular polarization images to derive the wavefront by an analytical approach. The NZPR only operates in the small aberration regime. Deep Learning Phase Retrieval methods (DLPR; Quesnel et al. 2020) also use the vortex phase to break the sign ambiguity, but extend the use beyond the small phase regime by using machine learning techniques. Then, there are also techniques that put a photonic lantern in the focal plane. A photonic lantern is a device that splits a multimode fiber into multiple single-mode fibers. In the photonic lantern, the focal-plane electric field is mixed in the multimode fiber and then filtered by the single-mode fibers such that from its output the different electric field components can be reconstructed. One of these single-mode fibers can feed a high-resolution spectrograph, while the output of the other single-mode fibers can be used for wavefront sensing. The first implementation only focussed on detecting pointing errors (Corrigan et al., 2018), but it was recently demonstrated that higher-order wavefront aberrations can also be measured (Norris et al., 2020).

Pupil-plane manipulation
The pupil-plane manipulation is the largest branch of the family tree shown in Figure 1.7. In subsection 1.3.1 we discussed how the pupil-plane phase and amplitude should be manipulated to overcome the sign ambiguity. This branch can be divided into two smaller branches based on whether the FPWFS uses phase or amplitude manipulation. Starting

with the pupil-plane phase branch, the most well-known and used method is phase diversity (PD; Gonsalves 1982; Paxman et al. 1992). This method fits a non-linear image formation model to in- and out-of-focus PSFs to retrieve pupil-plane phase aberrations. PD has led to many other FPWFSs. For example, the COronagraphic Focal-plane waveFront Estimation for Exoplanet detection (COFEE; Paul et al. 2013) FPWFS includes a coronagraph to the image formation model for HCI observations. COFFEE was subsequently extended to also measure pupil-plane amplitude aberrations (Herscovici-Schiller et al., 2018), and include atmospheric turbulence in the model (Herscovici-Schiller et al., 2019). Linearized Analytical Phase Diversity or LAPD (Vievard et al., 2020) uses a linear approximation to measure the wavefront, and was mainly developed to co-phase segmented telescopes. LAPD is now also being tested to measure the LWE at Subaru/SCExAO (Vievard et al., 2019). Sequential-Phase Diversity (SPD; Gonsalves 2002) was developed to be able to run continuously in closed-loop, without defocussing the camera, by using the previous DM command as diversity and assuming that the algorithm operates in the small aberration regime. Fast and Furious (F&F; Keller et al. 2012; Korkiakoski et al. 2014) extends the regime in which SPD can operate by introducing a higher-order approximation of the PSF. F&F has been successfully tested on-sky in the context of measuring and correcting the LWE at Subaru/SCExAO (Chapter 6; Bos et al. 2020b). The NZPR and DLPR techniques described in the focal-plane manipulation branch are also used with phase diversity (Quesnel et al., 2020; Riaud et al., 2012b; van Haver et al., 2006). Then, the next focal-plane wavefront sensor in this branch is the Holographic Modal WaveFront Sensor (HMWFS; Wilby et al. 2017). Using a static optic, the HMWFS generates a number of PSF copy pairs, and each pair is biased with a pupil-plane phase mode with opposite sign. By monitoring the relative brightness of the PSF pairs, the magnitudes and signs of a set of pupil-plane modes can be measured. It was successfully tested during an observing run with WHT/LEXI (Haffert et al., 2018).

The following FPWFSs also belong to the pupil-plane manipulation branch, but focus on measuring the focal-plane electric field. Speckle Nulling (SN; Bordé & Traub 2006) singles out bright speckles in the coronagraphic image, and commands the DM to add artificial speckles on top of them. By alternating the phase of the artificial speckle and observing the combined brightness, SN finds the appropriate DM command to cancel the speckle. It has been successfully tested on-sky with Subaru/SCExAO (Martinache et al., 2014) and Keck/NIRC2 (Bottom et al., 2016), and is also used for space-based HCI experiments (Trauger & Traub, 2007). Pair-wise probing (PWP; Give'on et al. 2011) extends SN by simultaneously probing large parts of the focal-plane with DM commands. It is mainly considered for space-based observatories (Groff et al., 2015), but was recently also installed on VLT/SPHERE for on-sky tests (Potier et al., 2020b). PWP and the HMWFS are combined in the Holographic Electric Field Sensor (HEFS; Por & Keller 2016) as a static solution of PWP. Phase-shifting interferometry (PShI; Bottom et al. 2017; Guyon 2004) modulates the focal-plane intensity by moving a small part of the Lyot stop. Phase-sorting interferometry (PSoI; Codona et al. 2008) and the Frazin algorithm (FA; Frazin 2013) both use naturally occurring speckles due to the atmospheric turbulence to measure the focal-plane electric field. This requires them to combine milli-second exposure images with synchronized wavefront telemetry from the main WFS. The phase and am-

plitude of the atmospheric speckles are derived from the WFS measurements. The interference between the atmospheric speckles and more slowly evolving speckles originating from NCPA allows for measuring the phase and amplitude of the NCPA speckles.

There is also an entire class of FPWFSs that use pupil-plane amplitude manipulations. The Asymmetric Pupil Fourier WaveFront Sensor (APFWFS; Martinache 2013) uses an interferometric approach based on kernel phase analysis (Martinache, 2010) to retrieve the pupil-plane phase aberrations based on a non-coronagraphic PSF formed by an asymmetric pupil. It has seen multiple successful on-sky tests with Subaru/SCExAO (Martinache et al., 2016; N'Diaye et al., 2018). The Asymmetric Pupil vector-Apodizing Phase Plate or APvAPP (Chapter 2; Bos et al. 2019) is a pupil-plane coronagraph integrated with a pupil-plane amplitude asymmetry. The pupil-plane phase is retrieved with a non-linear coronagraphic model fitted to the coronagraphic image. This technique has also seen successful on-sky tests, and can be extended to measure pupil-plane amplitude aberrations as well (Bos et al., 2020a). Spatial Linear Dark Field Control (SpatLDFC; Miller et al. 2017) monitors the bright field opposite to the dark hole for intensity fluctuations generated by wavefront aberrations. This is because LDFC assumes that intensity fluctuations in the bright field have a linear response to wavefront aberrations, while those in the dark hole have a quadratic response. Using an empirical calibration, these intensity fluctuations are converted to appropriate DM commands to cancel aberrations. SpatLDFC is designed to be a wavefront stabilization technique, and cannot create a dark hole on its own. It is implemented both with pupil- and focal-plane coronagraphs. The coronagraph dictates the method that SpatLDFC relies on to break the sign ambiguity. For pupil-plane coronagraphs, such as the APvAPP, there is a bright coronagraphic PSF that requires an amplitude asymmetry to provide the diversity. SpatLDFC combined with an APvAPP has been successfully tested on the Subaru/SCExAO system with the internal source (Chapter 3; Miller et al. 2021) and on-sky (Chapter 4; Bos et al. submitted). For a focal-plane coronagraph, the bright field predominately consists of uncorrected wavefront aberrations that break the sign degeneracy. Laboratory experiments for space-bases observatories have been successfully performed in this context as well (Currie et al., 2020b).

The differential Optical Transfer Functions (dOTF; Codona 2013) uses a Fourier analysis on two images (one with and one without amplitude asymmetry) to retrieve the pupil-plane phase and amplitude aberrations. The asymmetry can also be introduced by a linear polarizer, which then requires a polarizing beam splitter to do the dOTF analysis. This is referred to as the polarization dOTF (pdOTF; Brooks et al. 2016).

The self-coherent camera (SCC; Baudoz et al. 2005) places a reference hole in an off-axis position of the coronagraph's Lyot stop. The reference hole transmits light that is diffracted by the coronagraph outside of the geometric pupil that would have otherwise been blocked by the Lyot stop. This light propagates to the focal plane, interferes with the on-axis beam, and generates high spatial-frequency fringes. The focal-plane electric field is spatially modulated and directly available through a Fourier analysis of the image. It has been tested at high contrasts for space-based systems (Potier et al., 2020a) and on-sky for ground-based systems (Galicher et al., 2019). The Fast Atmospheric SCC

Technique (FAST; Gerard & Marois 2020; Gerard et al. 2018, 2019) modifies the coronagraph's focal-plane optic such that the core of the PSF is diffracted onto the reference hole, drastically increasing the light available for wavefront sensing. Other variants of the SCC exist that combine the SCC with other FPWFS concepts. The fast-modulated SCC (FMSCC; Martinez 2019) effectively combines the dOTF concept with the SCC by temporally modulating the reference light. The polarization-encoded SCC (PESCC; Chapter 5; Bos 2021) has a similar combination with the pdOTF. Lastly, the spectral-modulated SCC (SMSCC; Haffert in prep.) encodes the reference hole in different spectral channels.

Spectral manipulation
Finally, there is a family of techniques that use spectral manipulations to estimate aberrations. For example, the Multispectral Exoplanet Detection Using Simultaneous Aberration Estimation (MEDUSAE; Ygouf et al. 2013) technique jointly estimates the wavefront aberrations and astronomical object given a multispectral dataset. MEDUSAE has currently only been tested as post-processing method, but also has the capability to be run in realtime for wavefront sensing. Spectral Linear Dark Field control (SpecLDFC; Guyon et al. 2017) is very similar to SpatLDFC, but instead of measuring the wavefront at a different location, it measures the wavefront using other wavelengths. SpecLDFC uses the linear relationship between the intensity of bright speckles outside of the science bandwidth and residual wavefront aberrations. By monitoring brightness changes of these speckles, it derives DM commands that correct for wavefront drifts.

1.4 This thesis

This thesis presents and validates new focal-plane wavefront sensors in theory, simulation, and on-sky tests, and introduces a new optic to enable the detection of exoplanet variability. The ultimate goal is to enable the direct imaging and characterization of rocky exoplanets with the future extremely large telescopes. The main focus of this thesis lies on developing integrated coronagraph and focal-plane wavefront-sensing solutions to measure and correct non-common path aberrations in high-contrast imaging instruments (Chapters 2 – 5). The last two chapters investigate on-sky tests of a focal-plane wavefront sensing solution to address the low-wind effect (Chapter 6), and a new concept to dramatically increase the signal-to-noise ratio of exoplanet variability measurements (Chapter 7).

Chapter 2: Focal-plane wavefront sensing with the vector-Apodizing Phase Plate coronagraph
This chapter introduces a novel focal-plane wavefront sensor by combining the vector-Apodizing Phase Plate (vAPP) coronagraph with an asymmetric pupil wavefront sensor. A non-linear, model-based wavefront sensing algorithm is presented as well. We study the performance of the vAPP and the wavefront-sensing algorithm in idealized simulations. Furthermore, the wavefront sensing capabilities are demonstrated on the Subaru/SCExAO system with the internal source and on-sky. For the on-sky tests, we report a raw contrast improvement of a factor $\sim$ 2 between 2 and 4 λ/D when measuring and controlling the thirty lowest Zernike modes.

Chapter 3 and 4: Spatial Linear Dark Field Control with the vector-Apodizing Phase Plate

These two chapters present the successful deployment of spatial Linear Dark Field Control (LDFC) to Subaru/SCExAO. LDFC assumes a linear relationship between intensity changes in some parts of the bright field of the vAPP coronagraphic PSF and changing wavefront aberrations. We show that, to successfully operate LDFC with the vAPP without defocus, an amplitude asymmetry needs to be integrated into the vAPP design.

Chapter 3 describes the implementation of LDFC at Subaru/SCExAO, including a noise analysis of LDFC's performance with the SCExAO vAPP. Furthermore, the results of lab tests are presented that simulate temporally-correlated, evolving phase aberrations with the deformable mirror (DM). We find that, when LDFC is operating in closed-loop, there is a factor of ~ 3 improvement in raw contrast across the dark hole during the full duration of the test.

Chapter 4 describes the results of the first successful LDFC on-sky tests. Two types of tests are presented: (1) correction of artificially introduced aberrations, and (2), correction of wavefront errors that originate from the telescope, instrument, and atmosphere. When introducing aberrations with the DM, we find that LDFC improves the raw contrast by a factor 3–7 over the dark hole by decreasing the residual wavefront error from ~ 90 nm to ~ 40 nm root mean square. For the second type of tests, we show that the current implementation of LDFC is able to suppress evolving aberrations with timescales $< 0.1 - 0.4$ Hz, and is limited by the current Python implementation. We find that the power at 10 mHz is reduced by factor $\sim$ 20, 7, and 4 for spatial frequency bins at 2.5, 5.5, and 8.5 λ/D, respectively.

Chapter 5: The polarization-encoded self-coherent camera

This chapter presents the polarization-encoded self-coherent camera (PESCC), an integrated focal-plane wavefront sensor and coronagraph, which is a new and powerful variant of the self-coherent camera (SCC). The PESCC implements a Lyot stop with a reference hole featuring a polarizer, and a downstream polarizing beamsplitter. We show that the PESCC relaxes the requirements on the optics size, focal-plane sampling, and spectral resolution with respect to the SCC. Furthermore, we find via numerical simulations that the PESCC has effectively access to ~ 16 times more photons, improving the wavefront sensing sensitivity by a factor ~ 4. We also show that, without additional measurements, coherent differential imaging (CDI) is enabled as a contrast-enhancing post-processing technique for every observation. In idealized simulations representative of space-based systems with a charge two vortex coronagraph, we show that wavefront sensing and control, combined with CDI, can achieve a 1σ raw contrast of $\sim 3 \cdot 10^{-11} - 8 \cdot 10^{-11}$ between 1 and 18 λ/D.

Chapter 6: Controlling the Low Wind Effect with Fast and Furious focal-plane wavefront sensing

This chapter presents the deployment of the Fast and Furious (F&F) focal-plane wavefront sensing algorithm to Subaru/SCExAO to measure and correct the low-wind effect (LWE). F&F is a sequential phase-diversity algorithm and a software-only solution to focal-plane

wavefront sensing. Tests with the internal source results show that F&F can correct a wide range of LWE-like aberrations and bring the PSF back to a high Strehl ratio (> 90%) and high symmetry. Furthermore, we present on-sky results that show that F&F is able to improve the PSF quality during very challenging atmospheric conditions (1.3 – 1.4" seeing at 500 nm). Simultaneous observations of the PSF in the optical (λ = 750 nm, $\Delta\lambda$ = 50 nm) show that we were correcting aberrations common to the optical and NIR paths within SCExAO.

Chapter 7: High-precision astrometry and photometry of directly imaged exoplanets with the Vector Speckle Grid

This chapter presents the theory and simulations of the vector speckle grid (VSG). The VSG is a new optical element to generate artificial speckles that serve as photometric and astrometric references when studying directly imaged exoplanets. We show, by imposing opposite amplitude or phase modulation on the opposite polarization states in the pupil plane, that artificial speckles are generated that are incoherent with the underlying speckle halo. This greatly increases the astrometric and photometric precision. In simulation we find that, for short-exposure images, the VSG reaches a $\sim 0.3 - 0.8\%$ photometric error and $\sim 3 - 10 \cdot 10^{-3}$ λ/D astrometric error, which is a performance improvement of a factor $\sim$ 20 and $\sim$ 5 compared to scalar variants, respectively. Furthermore, we outline how VSGs could be implemented using liquid-crystal technology to impose the geometric phase on the circular polarization states.

Bibliography

Aime, C., Soummer, R., & Ferrari, A. 2002, Astronomy & Astrophysics, 389, 334
Anglada-Escudé, G., Amado, P. J., Barnes, J., et al. 2016, Nature, 536, 437
Apai, D., Radigan, J., Buenzli, E., et al. 2013, The Astrophysical Journal, 768, 121
Apai, D., Kasper, M., Skemer, A., et al. 2016, The Astrophysical Journal, 820, 40
Apai, D., Biller, B., Burgasser, A., et al. 2019, Bulletin of the American Astronomical Society, 51, 204
Baranne, A., Queloz, D., Mayor, M., et al. 1996, Astronomy and Astrophysics Supplement Series, 119, 373
Barclay, T., Pepper, J., & Quintana, E. V. 2018, The Astrophysical Journal Supplement Series, 239, 2
Baudoz, P., Boccaletti, A., Baudrand, J., & Rouan, D. 2005, Proceedings of the International Astronomical Union, 1, 553
Berry, M. V. 1987, Journal of Modern Optics, 34, 1401
Beuzit, J.-L., Vigan, A., Mouillet, D., et al. 2019, Astronomy & Astrophysics, 631, A155
Biller, B. 2017, Astronomical Review, 13, 1
Biller, B., Apai, D., Bonnefoy, M., et al. 2021, arXiv preprint arXiv:2101.08514
Bloemhof, E., Dekany, R., Troy, M., & Oppenheimer, B. 2001, The Astrophysical Journal Letters, 558, L71
Boccaletti, A., Chauvin, G., Mouillet, D., et al. 2020, arXiv preprint arXiv:2003.05714
Bohn, A. J., Kenworthy, M. A., Ginski, C., et al. 2020, The Astrophysical Journal Letters, 898, L16
Bordé, P. J., & Traub, W. A. 2006, The Astrophysical Journal, 638, 488
Borucki, W. J., Koch, D., et al. 2010, in AAS/Division for Planetary Sciences Meeting Abstracts# 42, 47–03
Bos, S., Miller, K., Lozi, J., et al. submitted, Astronomy & Astrophysics
Bos, S. P. 2021, Astronomy & Astrophysics, 646, A177
Bos, S. P., Doelman, D. S., Miller, K. L., & Snik, F. 2020a, in Adaptive Optics Systems VII, Vol. 11448, International Society for Optics and Photonics, 114483W
Bos, S. P., Doelman, D. S., Lozi, J., et al. 2019, Astronomy & Astrophysics, 632, A48
Bos, S. P., Vievard, S., Wilby, M. J., et al. 2020b, arXiv preprint arXiv:2005.12097
Bottom, M., Femenia, B., Huby, E., et al. 2016, in Adaptive Optics Systems V, Vol. 9909, International Society for Optics and Photonics, 990955
Bottom, M., Wallace, J. K., Bartos, R. D., Shelton, J. C., & Serabyn, E. 2017, Monthly Notices of the Royal Astronomical Society, 464, 2937
Bowler, B., Sallum, S., Boss, A., et al. 2019, arXiv preprint arXiv:1903.06299
Brandt, T., Briesemeister, Z., Savransky, D., et al. 2019, Bulletin of the American Astronomical Society, 51, 269
Brooks, K. J., Catala, L., Kenworthy, M. A., Crawford, S. M., & Codona, J. L. 2016, in Advances in Optical and Mechanical Technologies for Telescopes and Instrumentation II, Vol. 9912, International Society for Optics and Photonics, 991203
Brown, A., Vallenari, A., Prusti, T., et al. 2018, Astronomy & astrophysics, 616, A1
Brown, A. G., Vallenari, A., Prusti, T., et al. 2016, Astronomy & Astrophysics, 595, A2
Cantalloube, F., Por, E., Dohlen, K., et al. 2018, Astronomy & Astrophysics, 620, L10
Cantalloube, F., Farley, O., Milli, J., et al. 2020, Astronomy and Astrophysics-A&A
Cantalloube, F., Gomez-Gonzalez, C., Absil, O., et al. 2021, arXiv preprint arXiv:2101.05080
Chauvin, G., Desidera, S., Lagrange, A.-M., et al. 2017, Astronomy & Astrophysics, 605, L9
Chilcote, J. K., Bailey, V. P., De Rosa, R., et al. 2018, in Ground-based and Airborne Instrumenta-

tion for Astronomy VII, Vol. 10702, International Society for Optics and Photonics, 1070244
Christiaens, V., Casassus, S., Absil, O., et al. 2019, Monthly Notices of the Royal Astronomical Society, 486, 5819
Codona, J. L. 2013, Optical Engineering, 52, 097105
Codona, J. L., & Angel, R. 2004, The Astrophysical Journal Letters, 604, L117
Codona, J. L., Kenworthy, M. A., & Lloyd-Hart, M. 2008, in Adaptive Optics Systems, Vol. 7015, International Society for Optics and Photonics, 70155D
Cooper, C. S., Sudarsky, D., Milsom, J. A., Lunine, J. I., & Burrows, A. 2003, The Astrophysical Journal, 586, 1320
Corrigan, M. K., Morris, T. J., Harris, R. J., & Anagnos, T. 2018, in Adaptive Optics Systems VI, Vol. 10703, International Society for Optics and Photonics, 107035H
Currie, T., Brandt, T. D., Kuzuhara, M., et al. 2020a, The Astrophysical Journal Letters, 904, L25
Currie, T., Pluzhnik, E., Guyon, O., et al. 2020b, Publications of the Astronomical Society of the Pacific, 132, 104502
Damasso, M., Del Sordo, F., Anglada-Escudé, G., et al. 2020, Science advances, 6, eaax7467
De Boer, J., Langlois, M., Van Holstein, R. G., et al. 2020, Astronomy & Astrophysics, 633, A63
De Kok, R., Stam, D., & Karalidi, T. 2011, The Astrophysical Journal, 741, 59
Doelman, D. S., Auer, F. F., Escuti, M. J., & Snik, F. 2019, Optics letters, 44, 17
Doelman, D. S., Por, E. H., Ruane, G., Escuti, M. J., & Snik, F. 2020, Publications of the Astronomical Society of the Pacific, 132, 045002
Doelman, D. S., Snik, F., Warriner, N. Z., & Escuti, M. J. 2017, in Techniques and Instrumentation for Detection of Exoplanets VIII, Vol. 10400, International Society for Optics and Photonics, 104000U
Eisenhauer, F., Abuter, R., Bickert, K., et al. 2003, in Instrument Design and Performance for Optical/Infrared Ground-based Telescopes, Vol. 4841, International Society for Optics and Photonics, 1548–1561
Eriksson, S. C., Janson, M., & Calissendorff, P. 2019, Astronomy & Astrophysics, 629, A145
Escuti, M. J., Kim, J., & Kudenov, M. W. 2016, Optics and Photonics News, 27, 22
Frazin, R. A. 2013, The Astrophysical Journal, 767, 21
Fried, D. L. 1966, JOSA, 56, 1372
Galicher, R., Baudoz, P., Delorme, J.-R., et al. 2019, Astronomy & Astrophysics, 631, A143
Gerard, B. L., & Marois, C. 2020, Publications of the Astronomical Society of the Pacific, 132, 064401
Gerard, B. L., Marois, C., & Galicher, R. 2018, The Astronomical Journal, 156, 106
Gerard, B. L., Marois, C., Galicher, R., et al. 2019, arXiv preprint arXiv:1910.04554
Give'on, A., Kern, B. D., & Shaklan, S. 2011, in Techniques and Instrumentation for Detection of Exoplanets V, Vol. 8151, International Society for Optics and Photonics, 815110
Goebel, S. B., Guyon, O., Hall, D. N., et al. 2018, Publications of the Astronomical Society of the Pacific, 130, 104502
Gonsalves, R. A. 1982, Optical Engineering, 21, 215829
Gonsalves, R. A. 2002, in European Southern Observatory Conference and Workshop Proceedings, Vol. 58, 121
Goodman, J. W. 2005, Introduction to Fourier optics (Roberts and Company Publishers)
Greenwood, D. P. 1977, JOSA, 67, 390
Groff, T. D., Riggs, A. E., Kern, B., & Kasdin, N. J. 2015, Journal of Astronomical Telescopes, Instruments, and Systems, 2, 011009
Guyon, O. 2004, The Astrophysical Journal, 615, 562
—. 2005, The Astrophysical Journal, 629, 592
—. 2018, Annual Review of Astronomy and Astrophysics, 56, 315

Guyon, O., Martinache, F., Cady, E. J., et al. 2012, in Adaptive Optics Systems III, Vol. 8447, International Society for Optics and Photonics, 84471X
Guyon, O., Mazin, B., Fitzgerald, M., et al. 2018, in Adaptive Optics Systems VI, Vol. 10703, International Society for Optics and Photonics, 107030Z
Guyon, O., Miller, K., Males, J., Belikov, R., & Kern, B. 2017, arXiv preprint arXiv:1706.07377
Haffert, S., Bohn, A., de Boer, J., et al. 2019, Nature Astronomy, 3, 749
Haffert, S., Wilby, M., Keller, C., et al. 2018, in Society of Photo-Optical Instrumentation Engineers (SPIE) Conference Series, Vol. 10703, SPIE
Haffert, S. Y. in prep.
Hardy, J. W. 1998, Adaptive optics for astronomical telescopes, Vol. 16 (Oxford University Press on Demand)
Hartmann, J. 1900, Zeitschrift für Instrumentenkunde, 20, 47
Helling, C. 2019, Annual Review of Earth and Planetary Sciences, 47, 583
Henry, G. W., Marcy, G. W., Butler, R. P., & Vogt, S. S. 1999, The Astrophysical Journal Letters, 529, L41
Herscovici-Schiller, O., Mugnier, L. M., Baudoz, P., et al. 2018, Astronomy & Astrophysics, 614, A142
Herscovici-Schiller, O., Sauvage, J.-F., Mugnier, L. M., Dohlen, K., & Vigan, A. 2019, Monthly Notices of the Royal Astronomical Society, 488, 4307
Hinkley, S., Oppenheimer, B. R., Soummer, R., et al. 2007, The Astrophysical Journal, 654, 633
Hoeijmakers, H., Schwarz, H., Snellen, I., et al. 2018, Astronomy & Astrophysics, 617, A144
Holzlöhner, R., Kimeswenger, S., Kausch, W., & Noll, S. 2020, arXiv preprint arXiv:2010.01978
Huby, E., Baudoz, P., Mawet, D., & Absil, O. 2015, Astronomy & Astrophysics, 584, A74
Huby, E., Bottom, M., Femenia, B., et al. 2017, Astronomy & Astrophysics, 600, A46
Jacob, W. 1855
Jovanovic, N., Guyon, O., Martinache, F., et al. 2015a, The Astrophysical Journal Letters, 813, L24
Jovanovic, N., Martinache, F., Guyon, O., et al. 2015b, Publications of the Astronomical Society of the Pacific, 127, 890
Jovanovic, N., Absil, O., Baudoz, P., et al. 2018, arXiv preprint arXiv:1807.07043
Karalidi, T., Stam, D., & Hovenier, J. 2012, Astronomy & Astrophysics, 548, A90
Kasdin, N. J., Vanderbei, R. J., Spergel, D. N., & Littman, M. G. 2003, The Astrophysical Journal, 582, 1147
Keller, C. U., Korkiakoski, V., Doelman, N., et al. 2012, in Adaptive Optics Systems III, Vol. 8447, International Society for Optics and Photonics, 844721
Keppler, M., Benisty, M., Müller, A., et al. 2018, Astronomy & Astrophysics, 617, A44
Komanduri, R. K., Lawler, K. F., & Escuti, M. J. 2013, Optics Express, 21, 404
Korkiakoski, V., Keller, C. U., Doelman, N., et al. 2014, Applied optics, 53, 4565
Kostov, V., & Apai, D. 2012, The Astrophysical Journal, 762, 47
Kuhn, J., Potter, D., & Parise, B. 2001, The Astrophysical Journal Letters, 553, L189
Langlois, M., Vigan, A., Moutou, C., et al. 2013, in Proceedings of the Third AO4ELT Conference, 63
Langlois, M., Dohlen, K., Vigan, A., et al. 2014, in Ground-based and Airborne Instrumentation for Astronomy V, Vol. 9147, International Society for Optics and Photonics, 91471R
Le Louarn, M., Béchet, C., & Tallon, M. 2013, in Proc. of the Third AO4ELT Conference
Lindegren, L., Babusiaux, C., Bailer-Jones, C., et al. 2007, Proceedings of the International Astronomical Union, 3, 217
Lyot, B. 1939, Monthly Notices of the Royal Astronomical Society, 99, 580
Macintosh, B., Poyneer, L., Sivaramakrishnan, A., & Marois, C. 2005, in Astronomical Adaptive Optics Systems and Applications II, Vol. 5903, International Society for Optics and Photonics,

59030J
Macintosh, B., Graham, J. R., Ingraham, P., et al. 2014, Proceedings of the National Academy of Sciences, 111, 12661
Macintosh, B., Graham, J., Barman, T., et al. 2015, Science, 350, 64
Madec, P.-Y. 2012, in Adaptive Optics Systems III, Vol. 8447, International Society for Optics and Photonics, 844705
Males, J. R., Belikov, R., & Bendek, E. 2015, in Techniques and Instrumentation for Detection of Exoplanets VII, Vol. 9605, International Society for Optics and Photonics, 960518
Marois, C., Lafreniere, D., Doyon, R., Macintosh, B., & Nadeau, D. 2006a, The Astrophysical Journal, 641, 556
Marois, C., Lafreniere, D., Macintosh, B., & Doyon, R. 2006b, The Astrophysical Journal, 647, 612
Marois, C., Macintosh, B., Barman, T., et al. 2008, science, 322, 1348
Martinache, F. 2010, The Astrophysical Journal, 724, 464
—. 2013, Publications of the Astronomical Society of the Pacific, 125, 422
Martinache, F., Jovanovic, N., & Guyon, O. 2016, Astronomy & Astrophysics, 593, A33
Martinache, F., Guyon, O., Jovanovic, N., et al. 2014, Publications of the Astronomical Society of the Pacific, 126, 565
Martinez, P. 2019, Astronomy & Astrophysics, 629, L10
Martinez, P., Kasper, M., Costille, A., et al. 2013, Astronomy & Astrophysics, 554, A41
Martinez, P., Loose, C., Carpentier, E. A., & Kasper, M. 2012, Astronomy & Astrophysics, 541, A136
Mawet, D., Riaud, P., Absil, O., & Surdej, J. 2005, The Astrophysical Journal, 633, 1191
Mawet, D., Pueyo, L., Lawson, P., et al. 2012, in Space Telescopes and Instrumentation 2012: Optical, Infrared, and Millimeter Wave, Vol. 8442, International Society for Optics and Photonics, 844204
Mayor, M., & Queloz, D. 1995, Nature, 378, 355
Metchev, S. A., Heinze, A., Apai, D., et al. 2015, The Astrophysical Journal, 799, 154
Miller, K., Guyon, O., & Males, J. 2017, Journal of Astronomical Telescopes, Instruments, and Systems, 3, 049002
Miller, K., Bos, S., Lozi, J., et al. 2021, Astronomy & Astrophysics, 646, A145
Milli, J., Banas, T., Mouillet, D., et al. 2016, in Adaptive Optics Systems V, Vol. 9909, International Society for Optics and Photonics, 99094Z
Milli, J., Kasper, M., Bourget, P., et al. 2018, in Adaptive Optics Systems VI, Vol. 10703, International Society for Optics and Photonics, 107032A
Miskiewicz, M. N., & Escuti, M. J. 2014, Optics Express, 22, 12691
N'Diaye, M., Dohlen, K., Fusco, T., & Paul, B. 2013, Astronomy & Astrophysics, 555, A94
N'Diaye, M., Martinache, F., Jovanovic, N., et al. 2018, Astronomy & Astrophysics, 610, A18
N'Diaye, M., Vigan, A., Dohlen, K., et al. 2016, Astronomy & Astrophysics, 592, A79
Nielsen, E. L., De Rosa, R. J., Macintosh, B., et al. 2019, The Astronomical Journal, 158, 13
Norris, B. R., Wei, J., Betters, C. H., Wong, A., & Leon-Saval, S. G. 2020, arXiv preprint arXiv:2003.05158
Oh, C., & Escuti, M. J. 2008, Optics letters, 33, 2287
Otten, G. P., Snik, F., Kenworthy, M. A., et al. 2014, in Advances in Optical and Mechanical Technologies for Telescopes and Instrumentation, Vol. 9151, International Society for Optics and Photonics, 91511R
Pancharatnam, S. 1956, in Proceedings of the Indian Academy of Sciences-Section A, Vol. 44, Springer, 398–417
Patty, C. L., Ten Kate, I. L., Buma, W. J., et al. 2019, Astrobiology, 19, 1221

Paul, B., Mugnier, L., Sauvage, J.-F., Dohlen, K., & Ferrari, M. 2013, Optics Express, 21, 31751
Paxman, R. G., Schulz, T. J., & Fienup, J. R. 1992, JOSA A, 9, 1072
Perryman, M., Hartman, J., Bakos, G. Á., & Lindegren, L. 2014, The Astrophysical Journal, 797, 14
Petigura, E. A., Howard, A. W., & Marcy, G. W. 2013, Proceedings of the National Academy of Sciences, 110, 19273
Por, E. H. 2020, The Astrophysical Journal, 888, 127
Por, E. H., & Keller, C. U. 2016, in Adaptive Optics Systems V, Vol. 9909, International Society for Optics and Photonics, 990959
Potier, A., Baudoz, P., Galicher, R., Singh, G., & Boccaletti, A. 2020a, Astronomy & Astrophysics, 635, A192
Potier, A., Galicher, R., Baudoz, P., et al. 2020b, arXiv preprint arXiv:2005.02179
Quesnel, M., de Xivry, G. O., Louppe, G., & Absil, O. 2020, in Adaptive Optics Systems VII, Vol. 11448, International Society for Optics and Photonics, 114481G
Racine, R., Walker, G. A., Nadeau, D., Doyon, R., & Marois, C. 1999, Publications of the Astronomical Society of the Pacific, 111, 587
Ragazzoni, R. 1996, Journal of modern optics, 43, 289
Riaud, P., Mawet, D., & Magette, A. 2012a, Astronomy & Astrophysics, 545, A151
—. 2012b, Astronomy & Astrophysics, 545, A150
Ricker, G. R., Winn, J. N., Vanderspek, R., et al. 2014, Journal of Astronomical Telescopes, Instruments, and Systems, 1, 014003
Roddier, F., & Roddier, C. 1997, Publications of the Astronomical Society of the Pacific, 109, 815
Ruane, G., Riggs, A., Mazoyer, J., et al. 2018, in Space Telescopes and Instrumentation 2018: Optical, Infrared, and Millimeter Wave, Vol. 10698, International Society for Optics and Photonics, 106982S
Sahoo, A., Guyon, O., Lozi, J., et al. 2020, The Astronomical Journal, 159, 250
Sauvage, J.-F., Fusco, T., Guesalaga, A., et al. 2015, in Adaptive Optics for Extremely Large Telescopes 4–Conference Proceedings, Vol. 1
Sauvage, J.-F., Fusco, T., Lamb, M., et al. 2016, in Adaptive Optics Systems V, Vol. 9909, International Society for Optics and Photonics, 990916
Shack, R. V. 1971, J. Opt. Soc. Am., 61, 656
Singh, G., Lozi, J., Jovanovic, N., et al. 2017, Publications of the Astronomical Society of the Pacific, 129, 095002
Singh, G., Martinache, F., Baudoz, P., et al. 2014, Publications of the Astronomical Society of the Pacific, 126, 586
Singh, G., Lozi, J., Guyon, O., et al. 2015, Publications of the Astronomical Society of the Pacific, 127, 857
Sivaramakrishnan, A., & Oppenheimer, B. R. 2006, The Astrophysical Journal, 647, 620
Smith, B. A., & Terrile, R. J. 1984, Science, 226, 1421
Snellen, I., & Brown, A. 2018, Nature Astronomy, 2, 883
Snellen, I., de Kok, R., Birkby, J., et al. 2015, Astronomy & Astrophysics, 576, A59
Snik, F., Otten, G., Kenworthy, M., et al. 2012, in Modern Technologies in Space-and Ground-based Telescopes and Instrumentation II, Vol. 8450, International Society for Optics and Photonics, 84500M
Soummer, R., Aimé, C., & Falloon, P. 2003, Astronomy & Astrophysics, 397, 1161
Soummer, R., Ferrari, A., Aime, C., & Jolissaint, L. 2007, The Astrophysical Journal, 669, 642
Sparks, W. B., & Ford, H. C. 2002, The Astrophysical Journal, 578, 543
Stam, D., Hovenier, J., & Waters, L. 2004, Astronomy & Astrophysics, 428, 663
Stolker, T., Min, M., Stam, D. M., et al. 2017, Astronomy & Astrophysics, 607, A42

Struve, O. 1952, The Observatory, 72, 199
Tallis, M., Bailey, V. P., Macintosh, B., et al. 2020, Journal of Astronomical Telescopes, Instruments, and Systems, 6, 015002
Traub, W. A., & Oppenheimer, B. R. 2010, Exoplanets, 111
Trauger, J. T., & Traub, W. A. 2007, Nature, 446, 771
van Haver, S., Braat, J. J., Dirksen, P., & Janssen, A. J. 2006, Journal of the European Optical Society-Rapid publications, 1
van Holstein, R., Stolker, T., Jensen-Clem, R., et al. 2021, Astronomy & Astrophysics
van Holstein, R. G., Snik, F., Girard, J. H., et al. 2017, in Techniques and Instrumentation for Detection of Exoplanets VIII, Vol. 10400, International Society for Optics and Photonics, 1040015
Vievard, S., Bonnefois, A., Cassaing, F., Montri, J., & Mugnier, L. 2020, arXiv preprint arXiv:2011.10696
Vievard, S., Bos, S., Cassaing, F., et al. 2019, arXiv preprint arXiv:1912.10179
Vigan, A., N'Diaye, M., Dohlen, K., et al. 2019, Astronomy & Astrophysics, 629, A11
Vigan, A., Fontanive, C., Meyer, M., et al. 2020, arXiv preprint arXiv:2007.06573
Wagner, K., Follete, K. B., Close, L. M., et al. 2018, The Astrophysical Journal Letters, 863, L8
Wang, J. J., Rajan, A., Graham, J. R., et al. 2014, in Ground-based and Airborne Instrumentation for Astronomy V, Vol. 9147, International Society for Optics and Photonics, 914755
Wilby, M. J., Keller, C. U., Snik, F., Korkiakoski, V., & Pietrow, A. G. 2017, Astronomy & Astrophysics, 597, A112
Winn, J. N., & Fabrycky, D. C. 2015, Annual Review of Astronomy and Astrophysics, 53
Wolszczan, A., & Frail, D. A. 1992, Nature, 355, 145
Ygouf, M., Mugnier, L. M., Mouillet, D., Fusco, T., & Beuzit, J.-L. 2013, Astronomy & Astrophysics, 551, A138
Zhou, Y., Apai, D., Schneider, G. H., Marley, M. S., & Showman, A. P. 2016, The Astrophysical Journal, 818, 176